Acta Cryst. (1996). A**52**, 158–170

Detection of a Point Defect in a Silicon Single Crystal by a Subtraction Method using High-Resolution Transmission Electron Microscopy

M. Awaji[a,b]† and H. Hashimoto[b]

[a]*Department of Materials, University of Oxford, Parks Road, Oxford OX1 3PH, England, and* [b]*Faculty of Engineering, Okayama University of Science, Ridai-cho 1-1, Okayama 700, Japan*

(Received 20 January 1994; accepted 11 September 1995)

Abstract

The contrast of high-resolution transmission electron-microscope (HRTEM) images of silicon single crystals in $[\bar{1}10]$ orientation containing a pair of single $\langle 111 \rangle$ vacancies tetrahedrally bonded (divacancy), triple divacancy clusters in two orientations and an interstitial single Si atom has been calculated. The displacement of atoms around a point defect are deduced by extrapolating the distortion around a stacking-fault tetrahedron (SFT). The small contrast changes and displacements of the images of atoms in the crystal containing a point defect are revealed by finding the difference between the computed image of the point defect and that from the perfect crystal. The visibility of the images and the possibility of the detection of point defects are also discussed.

1. Introduction

Since it is well known that crystal lattice defects, such as point, line, planar and volume defects, play important roles in the properties of various crystalline materials, it is very important to observe such defects in materials. Although the observation of line, planar and volume defects by TEM has been observed extensively (Hirsch, Howie, Nicholson, Pashley & Whelan, 1965), only a limited number of reports on the observation of point defects have been published.

Krakow, Chang & Sass (1977) reported the observation of images of point defects at the atomic scale using the tilted-beam dark-field-imaging method and discussed the image contrast of the defect region using the kinematical theory of electron diffraction and compared it with observations. Though the dark-field images formed by using only limited regions of diffuse scattering were effective to obtain the image contrast of point defects with high contrast, the resolution of the observed images was not sufficient to discriminate the individual atomic images. In order to observe the small defects in silicon with atomic resolution, Zakharov, Pasemann & Rozhanski (1982) and Takai, Zakharov & Hashimoto (1982) used the multibeam dark-field-imaging method, in which the optical axis is located at the centre of several diffracted beams contributing to the images. To overcome the low intensity of dark-field images, Takai, Zakharov & Hashimoto (1982) used high-sensitivity photographic film and a high-sensitivity TV camera for recording the images and also used a high-brightness electron gun with LaB_6 filament. For observing the images of point defects in gold at the atomic level by high resolution and with sufficient brightness, Hashimoto, Takai, Ajika, Yokota & Endoh (1982) and Takai, Ajika & Hashimoto (1982) applied a tilted-beam aberration-free focus (AFF) condition, in which the optical axis is located at the centre of the primary undiffracted beam and the diffracted beams. The dark-field images are generally disturbed by quantum noise and the movement of atoms during an exposure, which causes misleading interpretation of the images of point defects. Recent improvements of image resolution to about 0.15–0.10 nm have made it possible to record the images using axial illumination and the multibeam imaging method. This method gives bright and high-resolution images. Therefore, multibeam imaging is useful to observe the images of point defects with high resolution and low noise. However, a calculated image contrast is necessary to identify the observed images. The calculated image contrast considering the distortion first around a single vacancy and then around a small SFT of interstitial or vacancy type in a thin gold crystal has been studied by Hashimoto *et al.* (1982) and Takai, Ajika & Hashimoto (1982) and more details were reported by Ajika, Hashimoto & Takai (1985). They showed the intensity distribution at the bottom surface corresponding to the images of vacancies and SFT at different depth positions in the crystal and for different thicknesses, and compared it with the observed images. Coene, Bender & Amelinckx (1985) also observed SFT in ion-implanted silicon and discussed the structure of a SFT by considering the Saldin–Whelan (1979) lattice distortion around the SFT. Fields & Cowley (1978) calculated image contrast of a split interstitial-type defect taking into account the lattice distortion in the atomic slice in which the defect is situated and discussed the

† Present address: National Research Institute for Metals, Sakura (Shibazaki) 3-13, Tsukuba, Ibaraki 305, Japan.

©1996 International Union of Crystallography
Printed in Great Britain – all rights reserved

dependence of the visibility on parameters used in the calculation. They suggested that point defects can be detected only in thin crystals of 0.5–2 nm thickness. A similar approach was carried out using the diffuse scattering of electrons by Glaisher & Spargo (1983), who considered the optimum imaging condition for obtaining the maximum visibility of a self-interstitial-type defect in silicon arising by changing the crystal thickness and the depth position of the defect and by considering the lattice distortion within the third-nearest neighbour of the defect. Bursill & Jun (1984*a*) reported from computer simulation that point defects should give an observable contrast for bright-field phase-contrast images of rutile. They also discussed the possibility of detecting small point defects in nonstoichiometric rutile from lattice images, using computer-image simulation without introducing the lattice distortion around the point defects, and concluded that, if the objective aperture is used to limit the image resolution to less than 0.23 nm, and the objective lens defocus and crystal thickness are close to Scherzer defocus and just beyond the first thickness extinction contour, respectively, then as few as three small aligned defects should be visible and, for higher-resolution images and other thicknesses, the lattice-image contrast overwhelms the contrast from the defects (Bursill & Jun, 1984*b*).

However, it is still difficult to know the real experimental values of parameters that produce the maximum visibility of point defects. For example, the defocus value can change during observation, specimen thickness, owing to surface roughness, cannot be determined as precisely as one atomic level and the depth of the point defect cannot be controlled to produce the maximum visibility. Therefore, it seems to be generally hopeless to observe point defects with sufficiently high contrast experimentally. Thus, it is desired to find a method of detecting the weak contrast of a point defect. In this paper, a subtraction technique is suggested for detecting the weak contrast of a point defect and of showing the limit of detection due to noise. As experimentally observed images are usually disturbed by some inevitable noise, HRTEM images and subtracted images are discussed by changing the noise level to examine the possibility of observation and identification of point defects with weak contrast.

2. Model of point defects and image calculation

Since the displacement of atoms around a point defect is not yet clearly known, the elastic strain field due to the SFT, which was proposed by Yoffe (1960) and Saldin & Whelan (1979), was extrapolated to the strain field of the point defects; in this calculation, the condition of the surface is not considered. The SFT is composed of four regular triangular dislocation loops (Yoffe, 1960) on (111) planes, and each of the loops is built up from three angular dislocation lines, whose displacements have been derived by Burgers (1939). The strain field U, V and W due to the angular dislocation line is expressed as follows:

$$U = b\varphi + b[xy/r(r-z) - x\eta/r(r-\zeta)]/8\pi(1-\sigma),$$

$$V = b\{\eta(\sin\alpha)/(r-\zeta) - y\eta/r(r-\zeta) + y^2/r(r-z) + (1-2\sigma)[(\cos\alpha)\ln(r-\zeta) - \ln(r-z)]\} \times [8\pi(1-\sigma)]^{-1},$$

$$W = b[\eta(\cos\alpha)/(r-\zeta) - y/r - \eta z/r(r-\zeta) - (1-2\sigma)(\sin\alpha)\ln(r-\zeta)]/8\pi(1-\sigma),$$

$$\varphi = \big[[\arctan(x/y)] - [\arctan(\eta/x)] + \big(\arctan\{xr(\sin\alpha)/[x^2(\cos\alpha) + y\eta]\}\big)\big]/4\pi,$$

where Burgers vector $\mathbf{b} = (b,0,0)$ and $P(x,y,z)$ or $P(x, \eta, \zeta)$ are two kinds of Cartesian coordinates of an arbitrary point P at which the displacement is to be calculated. The two coordinate systems x,y,z and x, η, ζ, whose origins are on each vertex of the triangular dislocation, are related to each other through a rotation angle α as follows:

$$\eta = y(\cos\alpha) - z(\sin\alpha),$$

$$\zeta = y(\sin\alpha) + z(\cos\alpha),$$

$$r^2 = x^2 + y^2 + z^2 = x^2 + \eta^2 + \zeta^2$$

and $\sigma = 0.22$ is the Poisson ratio of single-crystal silicon. Then, the strain field due to the SFT may be expressed as the summation of 12 angular dislocations after the transformation from x,y,z to crystal-lattice coordinates. In the present calculation, it is assumed that one divacancy is generated in (111) and $(\bar{1}11)$ planes by removing a pair of atoms bonded in the [111] and $[\bar{1}11]$ directions, respectively. This configuration of the divacancy was suggested from the result obtained using electron spin resonance (Corbett & Watkins, 1961). In order to take into account the strain field, a large unit cell (supercell) was adopted. The lattice parameters of the supercells are $A = 2.69$, $B = 2.72$ and $C = 0.38$ nm, $\alpha = \beta = \gamma = 90°$, and those of the fundamental unit cell are $a = b = c = 0.543$ nm, $\alpha = \beta = \gamma = 90°$. Fig. 1(*a*) shows the $[\bar{1}10]$ projection of the supercell containing a divacancy, which is marked by *—*, and the small rectangle represents a unit cell; Fig. 1(*b*) shows the perspective of the unit cell containing the divacancy. A pair of dotted circles numbered 4 and 5 represents the position of the divacancy, with each vacancy at the same depth from the top surface of the model crystal. In the diamond structure, if a single vacancy is produced, for example at the no. 5 atom position, the minimum size of the SFT consists of four (111) planes formed by numbered atoms 1–2–3, 2–3–4, 1–3–4 and 1–2–4. However, in the present case, the positions of atoms 4 and 5 are vacant. Since the diamond structure consists of two interpenetrating f.c.c. structures with the displacement $x = y = z = 1/4$, if the centres of gravity of the two corresponding displaced atoms are taken into

account, the diamond structure can be assumed to be f.c.c. By analogy with the f.c.c. structure, this divacancy may be assumed to be a single vacancy in the f.c.c. structure. So the minimum SFT can be assumed to have four Burgers vectors $\mathbf{b} = 1/12\langle 111 \rangle$ in the direction from inside to outside the SFT planes. Then, the position of

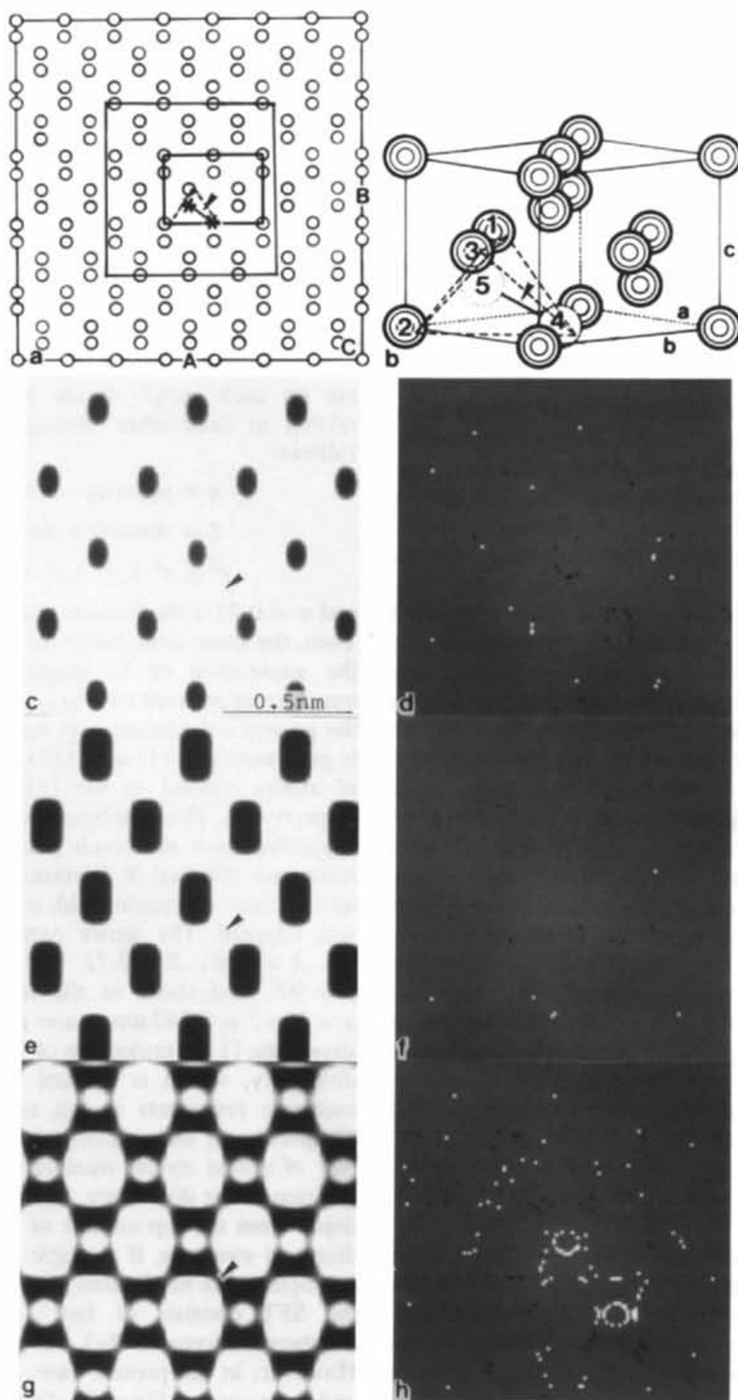

Fig. 1. Calculated image contrasts of the divacancy with bonding direction [111]. (*a*). Atom position projected on $(\bar{1}10)$. (*b*) Perspective of unit cell containing the divacancy numbered 4 and 5. (*c*), (*e*) and (*g*) are the calculated image contrasts of medium-size square in (*a*). (*d*), (*f*) and (*h*) are the subtracted images of (*c*), (*e*) and (*g*) from perfect single crystals.

each plane of the SFT can be determined after the collapse of the SFT and the outside matrix.

In the contrast calculation, to examine the possibility of *in situ* observation of the process of damage production by high-energy-electron-beam irradiation, the electron beam was made highly convergent to increase the current density per unit area. Thus, the multislice dynamical theory of electron diffraction and the image-formation theory concerning the effect of partial coherency of scattered waves were used with the following conditions: accelerating voltage = 800 kV; incident beam parallel to [$\bar{1}$10]; radius of the objective aperture = 3.7 nm^{-1}; number of excited waves in the crystal = 65536 (256 × 256); C_s (spherical aberration coefficient) = 2 mm; C_{ch} (chromatic aberration coefficient) = 3.4 nm; Δ_{ch} (chromatic defocus value) = 15 nm; Δf (underfocus value of the objective lens) = 50 nm; $\Delta\alpha$ (beam divergence semi-angle) = 1.46 mrad. These parameters coincide with the experimental condition of the electron-beam-irradiation work (Hashimoto *et al.*, 1991), which was done using the 1 MeV Atom Resolution Microscope at the Lawrence Berkeley Laboratory of the University of California.

3. Results and discussion

Figs. 1(*c*), (*e*) and (*g*) are the calculated images. The original calculated intensity level from 0 (minimum intensity) to 32 of maximum intensity level 255 was displayed to reveal the image-contrast change due to the divacancy clearly. Figs. 1(*d*), (*f*) and (*h*) are the subtracted images corresponding to the region shown by a square in the middle of Fig. 1(*a*). The position of the divacancy is also marked by arrows in Figs. 1(*c*), (*e*) and (*g*) and all the following calculated and subtracted images in Figs. 1 to 6 correspond to the square region. The depth position V nm of the divacancy over the thickness T nm of the model crystal (V/T) was adopted as (*c*) 3/5, (*e*) 8/10 and (*g*) 11/13 tentatively, *i.e.* the divacancy is located at 2 nm from the bottom surface but with various thicknesses of crystal above it. In Figs. 1(*c*), (*e*) and (*g*), the atom columns appear in dark contrast and the image contrast of the divacancy is rather difficult to see, but the numerically calculated contrasts of Figs. 1(*c*), (*e*) and (*g*) are 6.6, 5.4 and 3.9%. As the peak intensities within the projected SFT region are variable, the contrast is defined by the absolute value of the minimum or maximum value of the peak intensities that correspond to the defect position within the projected SFT region, *i.e.* $C = |(I_p - I_v)/I_p| \times 100$ (%), where I_v is the minimum or maximum value and I_p is the intensity at the same point in the perfect-crystal image that corresponds to I_v. The subtraction of two images of crystals with and without the point defect was carried out after adjusting both of the intensities of the images within the range of grey level from 0 (minimum intensity) to 128 (middle intensity) to 128, and those within the range from 129 to 255 (maximum intensity) to 160, *i.e.* both of the processed images have a rectangular intensity profile. Thus, the subtracted images between the rectangular intensity profiles become twinned arcs in two dimensions with black-and-white contrast on either side when the displacement of atom images has taken place and become rings with black or white contrast when the width of the rectangular intensity profile at the defect position changes from wide to narrow. As the images in Figs. 1(*c*) to (*h*) are plotted by the number of 129 × 129 pixels, the rimmed rings have a dotted structure. One dot corresponds to a pixel. It is rather difficult to see the displacement direction of the image of atom columns. However, the intensity differences in the contrast between the images of the perfect lattice and the crystal containing the divacancy at the atom columns, which appear as smaller intensity areas, are detected, as seen in Figs. 1(*d*) and (*h*) but not in (*f*). Fig. 2(*a*) shows a calculated image of a perfect crystal 20 nm thick and a pair of atom columns appears as one bright region. This and the following image intensities are displayed from minimum intensity (level 0) to maximum intensity (level 255). Fig. 2(*b*) shows the subtracted image of the same images, and this no contrast image means the subtraction process causes no error intensities. Figs. 2(*c*), (*e*) and (*g*) are images with V/T 3/20, 10/20 and 17/20, respectively, and Figs. 3, 4, 5 and 6 are also calculated with the same values of V/T. The calculated image contrasts in Figs. 2(*c*), (*e*) and (*g*) are 0.14, 1.6 and 0.13%. The change of image intensity is revealed in the subtracted images as white circles, and the displacement of the atom column images is revealed as semicircles. Comparison of Figs. 2(*d*), (*f*) and (*h*) shows that the white rings that appear at the positions corresponding to the images of atom columns that contain the divacancy are predominant. Thus, if the divacancy cannot be observed directly, the divacancy may be detected by this subtraction method when the noise level is sufficiently low. Fig. 3 shows the case of a divacancy directed parallel to the [$\bar{1}$11] direction; Figs. 3(*a*), (*b*) show the positions of the divacancy in the projection of the supercell and in the perspective of the unit cell. Figs. 3(*c*), (*e*) and (*g*) are the calculated images and the position of the divacancy is indicated by an arrow in each figure. The contrasts of the bright spots appearing at the divacancy position are 0.28, 4.0 and 0.68% for Figs. 3(*c*), (*e*) and (*g*). By comparing the image contrast of Fig. 3 with that of Fig. 2 numerically, it is seen that the image contrast of Fig. 3 is higher than that of Fig. 2, which is due to the difference of distortion based on the bonding direction of the divacancy, and the displacement field looks symmetrical about the position of the divacancy. It is seen that the subtracted image in Fig. 3(*h*) shows the position of the divacancy more clearly than is the case for Figs. 3(*d*) or (*f*). The subtracted images in Figs. 2 and 3 are more visible than those in Fig. 1. This seems to be because the images of atom pairs depicted in Fig. 1(*a*) appear as

bright spots in Figs. 2 and 3, whereas in Fig. 1 the atom positions are not distinguished but appear as an elongated dark region.

The second smallest SFT is formed by coagulation of triple divacancy clusters in the (111) plane, together with a displacement of a pair of atoms in the [111] direction as

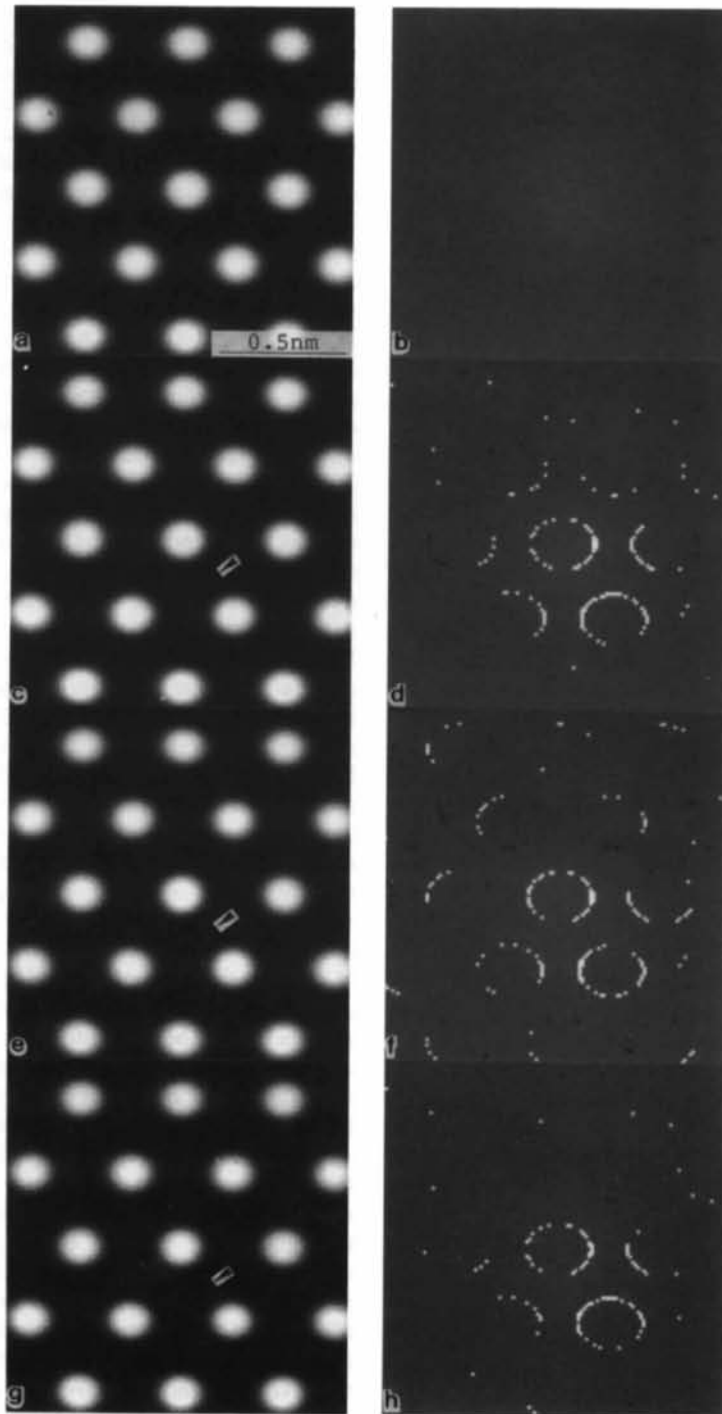

Fig. 2. Image contrasts depending on depth position V. The calculated image condition is the same as in Fig. 1 except $T = 20$ nm. (*a*) Perfect crystal, (*c*) $V = 3$ nm, (*e*) $V = 10$ nm, (*g*) $V = 17$ nm. Subtracted images: (*b*) perfect – (*a*), (*d*) perfect – (*c*), (*f*) perfect – (*e*), (*h*) perfect – (*g*).

shown in Figs. 4(*a*) and (*b*). In Fig. 4(*b*), a pair of atoms A–A' displaces to the position A'–A'' and the atom site A becomes vacant. It is assumed that the displacement Δ is $a \times 3^{1/2}/4$, so as to have equal spaces $\delta = a \times 3^{1/2}/12$ between each plane of the displaced tetrahedron and the plane of the matrix. By the collapse of the tetrahedron

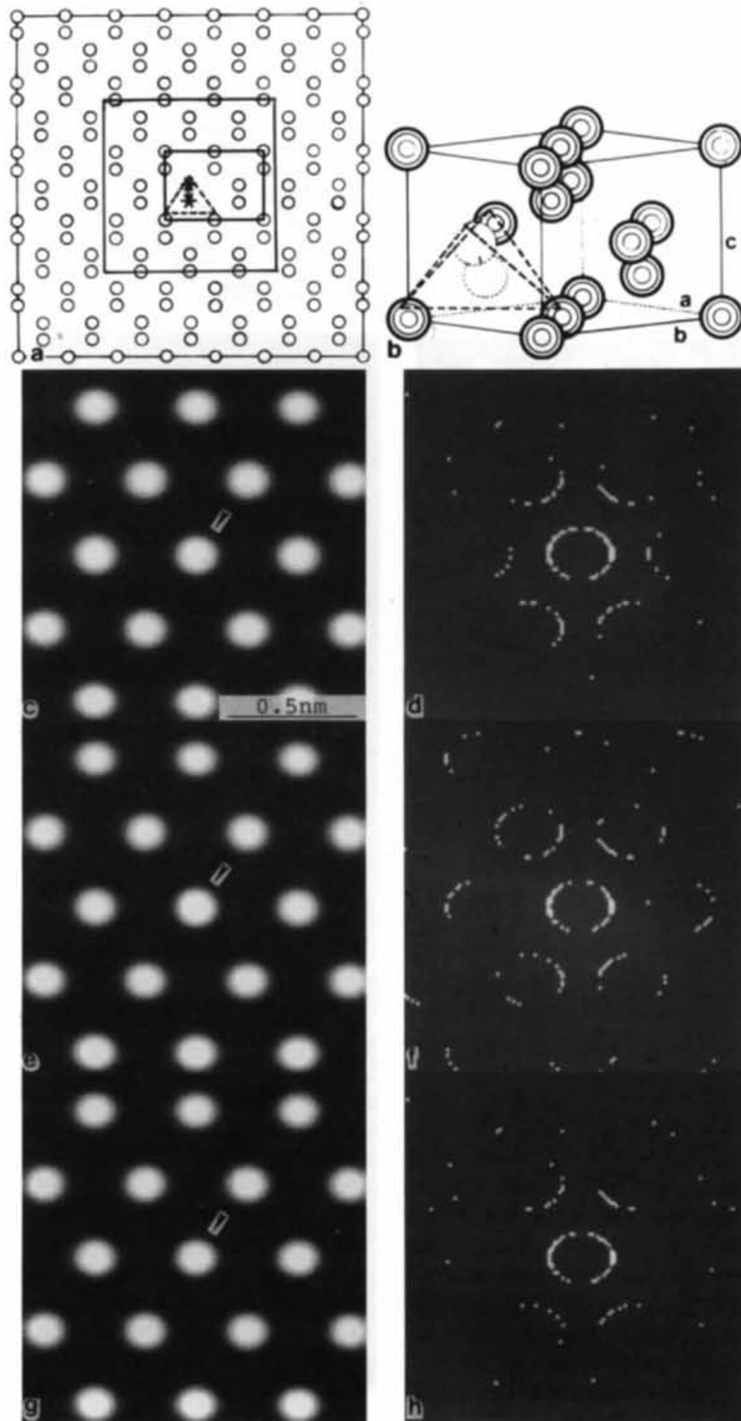

Fig. 3. One divacancy with bonding direction [$\bar{1}$11]. (*a*) Supercell, (*b*) unit cell. Other parameters and meanings are the same as in Fig. 2.

and the matrix, four boundary planes of the SFT are formed. The dotted lines in Figs. 4(*a*) and (*b*) show the SFT around the atoms A'–A''. Figs. 4(*c*), (*e*) and (*g*) are the calculated images of the SFT. The image contrasts at the SFT region are 1.1, 3.6 and 1.5%. The bright spots marked by arrows are smaller than the other bright ones,

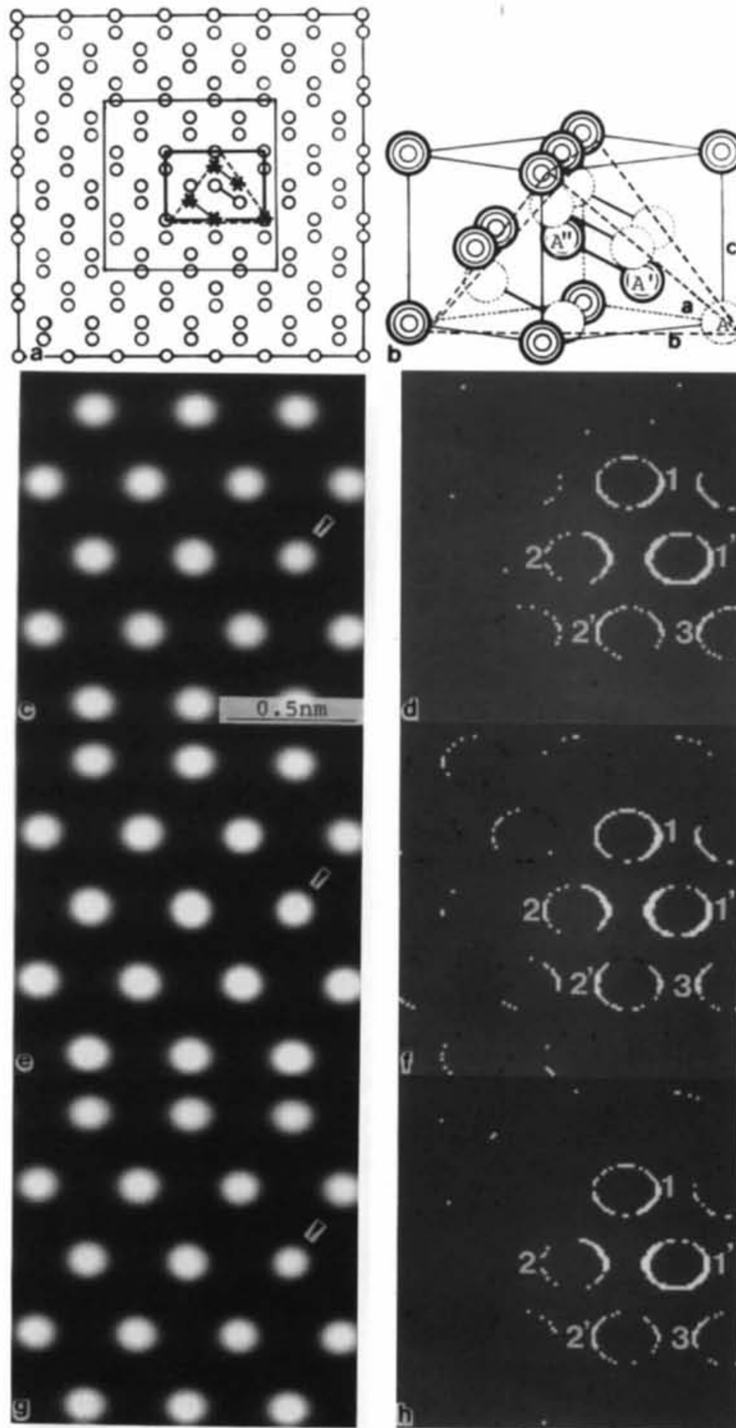

Fig. 4. Triple divacancy clusters with bonding direction [111]. Dotted lines show the second smallest SFT. (*a*) Supercell with the SFT, (*b*) unit cell with a pair of displaced atoms A'–A''.

so the image appears as if a divacancy oriented in the [$\bar{1}$11] direction exists at this region. But, as can be seen in the subtracted images, the intensity varies not only at the marked region but also in the surrounding atom columns 1, 1′, 2, 2′, 3, which contain atom vacancies as shown in Figs. 4(*a*) and (*b*). The white rings 1–1′ are clearer than

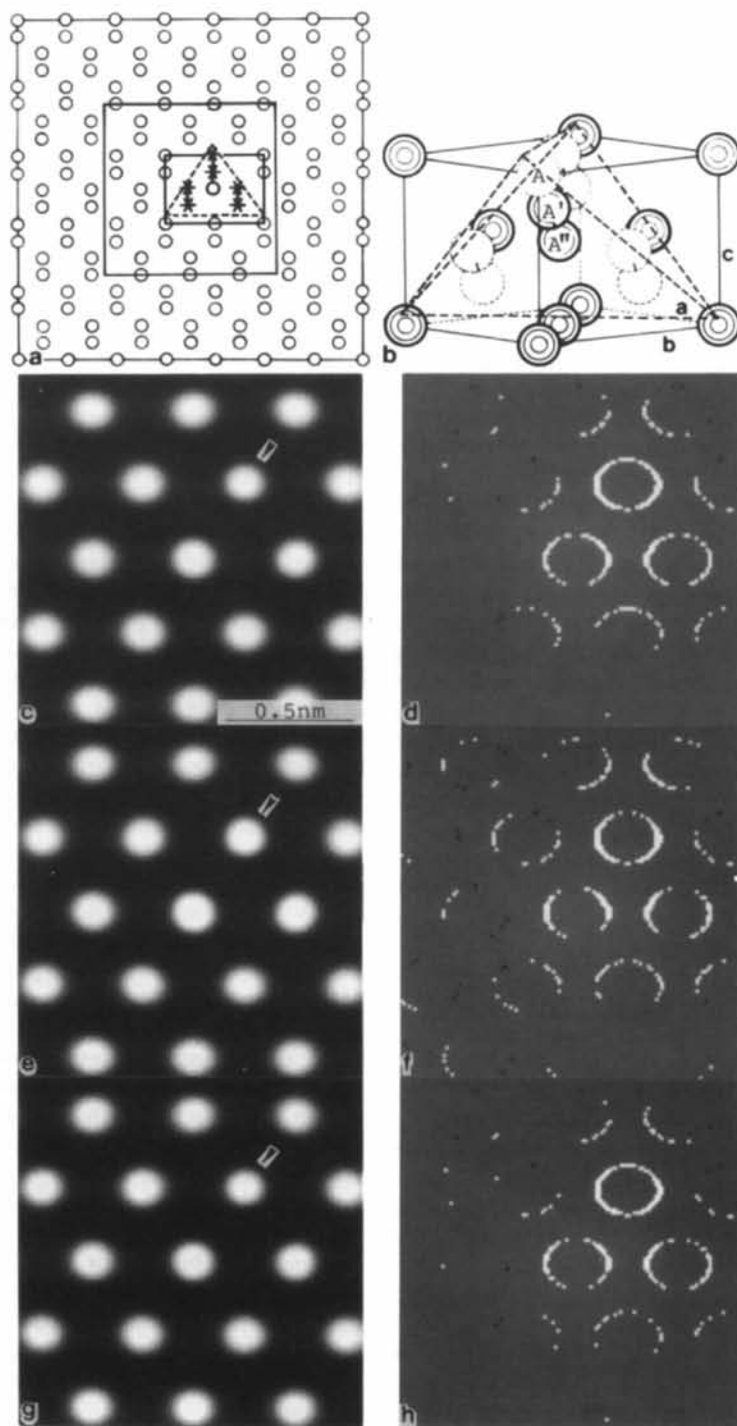

Fig. 5. Triple divacancy clusters with bonding direction [$\bar{1}$11]. (*a*) Supercell, (*b*) unit cell.

those of 2–2′ and 3, which seems to be due to the difference in the number of vacancies included in these atom columns. Fig. 5 shows the case of triple divacancy clusters parallel to the [$\bar{1}$11] direction. By the displacement of a pair of atoms from position A–A' to A'–A'' (Figs. 5*a*, *b*), the SFT is formed. The image contrasts at the SFT region shown in Figs. 5(*c*), (*e*) and (*g*) are 1.6, 6.3 and 2.1%. In these images, the projected position of the triple divacancy clusters appears as three small spots. In particular, the spots marked by arrows in each figure are the smallest. The spot marked corresponds to the superposed position of the upper divacancy and the single vacancy A as shown in Figs. 5(*a*) and (*b*). The white ring that corresponds to the marked spot in each subtracted image appears clearer than the others. This seems to be due to the number of vacancies in the projected direction. It is also seen that the width of the white rings is not uniform. This depends on the different distortions along the direction of the divacancy. By comparing the calculated image contrasts of Figs. 2, 3, 4 and 5, it is seen that the image contrasts of Fig. 3 and 5 are higher than those of Figs. 2 and 4. This is due to the difference in the orientation of the divacancies.

The image contrasts of the interstitial single atom of silicon are calculated and shown in Fig. 6. In this case (*i.e.* the case of an extrinsic stacking fault), it is assumed that the length of the edge of the SFT is equal to the diameter of a single Si atom, 0.234 nm, and the Burgers vector that produces the SFT has the same magnitude as the displacement for forming the divacancy (*i.e.* the case of an intrinsic stacking fault) but with opposite direction. The position of the interstitial atom is assumed to be at one of the four vacant tetrahedral positions [*i.e.* $x = y = 1/4$, $z = 3/4$ as shown in Figs. 6(*a*) and (*b*)]. In this tetrahedral position, the displacements of surrounding atoms seem to be negligibly small and no image-contrast change would be produced, but in the present treatment the silicon single crystal is assumed to be a homogeneous isotropic elasticity continuum, and thus the crystal is distorted by the interstitial atom. The arrows in Figs. 6(*c*), (*e*) and (*g*) indicate the atom position and the image contrasts at the interstitial atom position are 1.1, 3.1 and 3.0%. Though the intensity changes cannot be seen well, the subtracted images in Figs. 6(*d*), (*f*) and (*h*) reveal the displacement of the images of atom columns along the directions of the arrows. It is very difficult to detect the single-atom interstitial of silicon in this case because of its mobility, even at low temperature. It is also found that the displacement of the atoms in the matrix is of the order of 10^{-2} of atomic diameter and thus the image shift becomes of the order of 10^{-1}, but the atomic arrangement around a point defect could be well approximated by a tight-binding molecular-dynamics study rather than the present elastic distortion model.

From the experimental point of view, since the observed images usually contain not only contrast fluctuations due to quantum noise and surface conditions *etc.* but also fluctuations due to displaced atoms and movement of point defects, it is difficult to observe only a single vacancy or a single interstitial atom. For detecting a point defect with small contrast, the criteria for recognizability (Rose, 1948) of each bright-field and dark-field image contrast with noise are given by Saxton (1978) as

$$n \geq 25/c^2d^2 \quad \text{(bright-field image)},$$
$$n \geq 50/c^2d^2 \quad \text{(dark-field image)},$$

where n is the number of electrons incident on the specimen per unit area, c is the bright-field image contrast at a given point and d is the linear size of a resolution element. In practice, though, it is desirable to satisfy these inequalities for both bright-field and dark-field conditions, n is limited by the rate of damage of the specimen by the electron irradiation. If we calculate the doses required for imaging of the divacancy clusters in Fig. 4(*c*), substituting $c = 0.011$ and $d = 0.1$ mm in the case of bright-field imaging, we get the required electron doses as $n \geq 21 \times 10^6\,\text{mm}^{-2}$. Gibson & McDonald (1987) measured noise intensity with Si$\langle 110 \rangle$ thin films, which were made by a variety of specimen-preparation techniques. They obtained the result that the *in situ* cleaned specimen is clearly the best and is practically limited only by shot noise, since all surface contamination is removed by a 1473 K anneal *in situ* in an UHV electron microscope. It is impossible to observe the point defects without noise because other noise can also arise in the recording process owing to the quantized grain nature of the photographic plate *etc.* Fig. 7 shows the simulated images of the triple divacancy clusters (Fig. 4) with noise. In this figure, (*p*) indicates the calculated image without any defect but containing Gaussian noise. As the contrast is defined by maximum and minimum intensities, the noise level was changed from 1% (I) to 5% (V) of the intensity difference between $I_{\max}$ and $I_{\min}$ in the crystal-lattice image without noise and Figs. 7(*a*), (*b*), (*c*), (*d*), (*e*) and (*f*) correspond to Figs. 4(*c*), (*d*), (*e*), (*f*), (*g*) and (*h*). The noise was introduced following Gaussian statistics (Gibson & McDonald, 1987) by changing the intensity level. Even if the noise level is 1%, it is rather difficult to observe the contrast changes due to the defect in high-resolution images experimentally. But subtracted images show that, if the noise level is less than 3%, it should be possible to detect the position of the defect. A more accurate detection of a point defect with low contrast depends on the noise-elimination technique for high-resolution images. Thus, it may be concluded that the noise level in high-resolution images must be reduced to less than 3%, and the value of 3% or less may be a necessary experimental condition for detecting a point defect using this technique.

The above-mentioned discussion is concerned with the possibility of detection of point defects, which are

produced during the damage process by high-energy electron-beam irradiation. If we desire to observe the point defects statistically, the *in situ* cleaned specimen prepared in an UHV system must be irradiated by a high-energy electron beam and then observed with a sufficiently low acceleration voltage. The acceleration

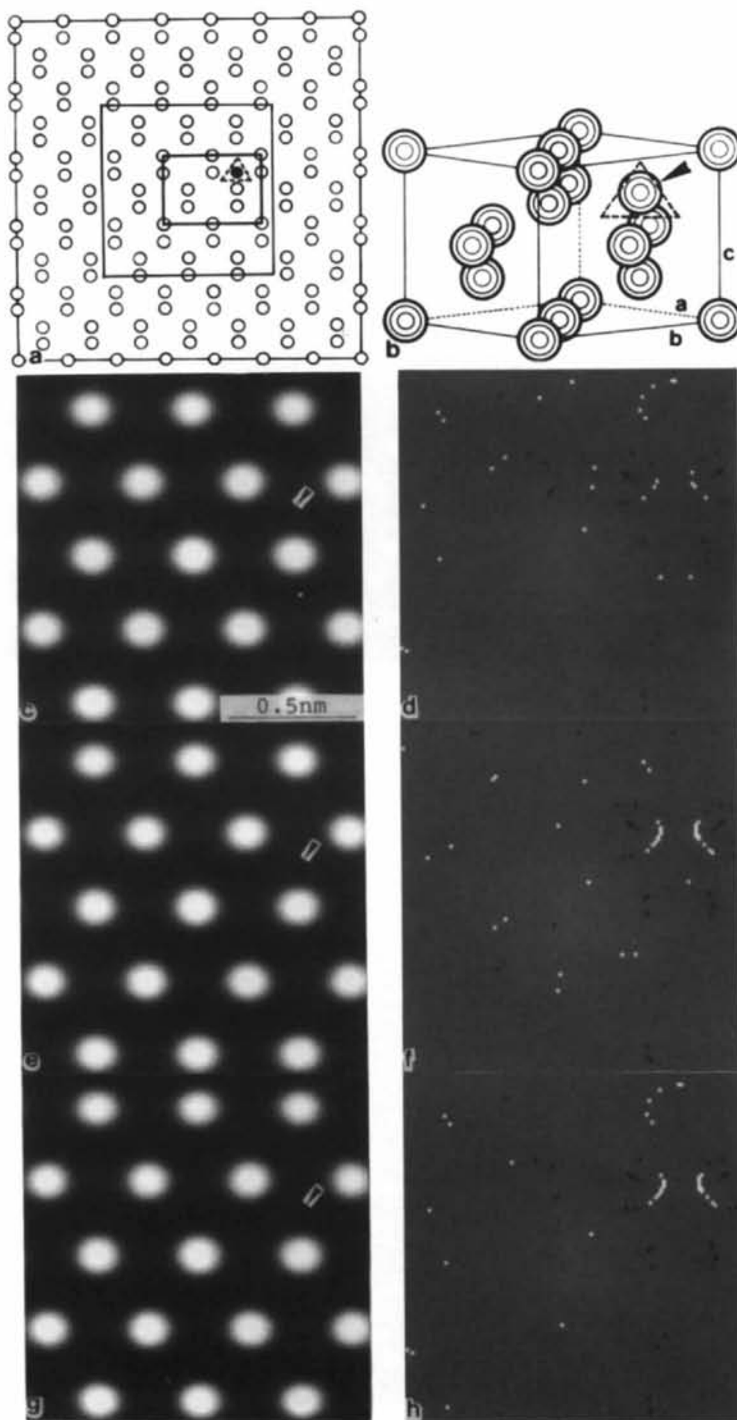

Fig. 6 Interstitial single atom of silicon at $x = y = 1/4$ and $z = 3/4$. (*a*) Supercell, (*b*) unit cell.

voltage can be determined by the cross section of the energy transfer from an electron to an atom in the knock-on collision process. The cross section for atom displacement is given by (Vinetskii & Kholodar, 1986)

$$\sigma_d(E, \mathbf{n}) = \int[\partial\sigma(E, E', \mathbf{n})/\partial E']G(E')\, dE', \qquad (1)$$

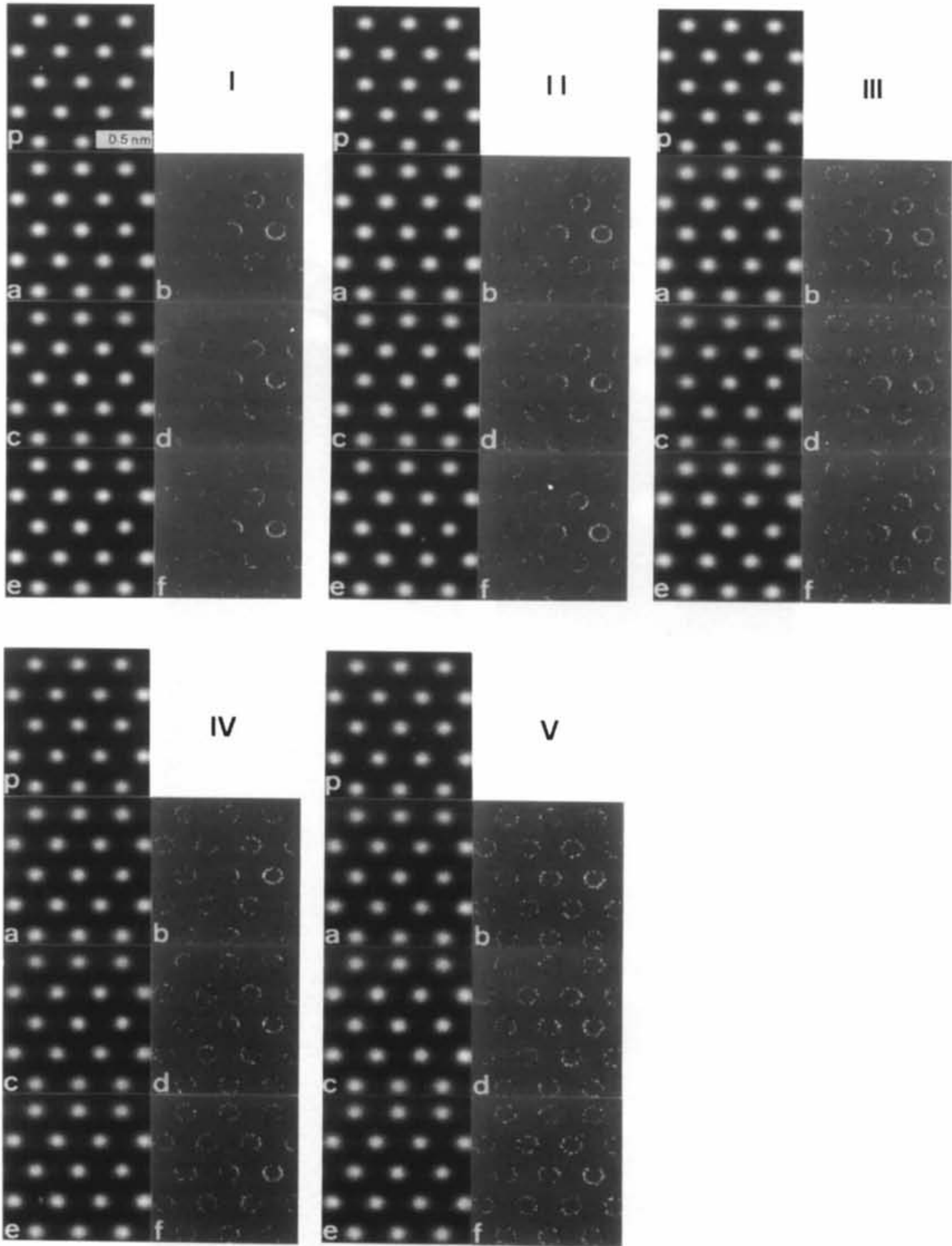

Fig. 7. Image contrasts of triple divacancy clusters with Gaussian noise in Fig. 4 and corresponding subtraction images. Noise levels change from 1% (I) to 5% (V).

where E is the incident electron energy, E' is the energy transferred from the electron to an atom in the crystal, $\mathbf{n}$ is a unit vector donating the direction of the incident electron, σ is the cross section of an atom that has this recoil energy and G is the probability that a given recoil energy produces a displacement. If we assume that the atom is bound to its site in the crystal lattice in an isotropic square-well potential of depth E_d, the threshold recoil energy, the function $G(E')$ gives the step-function threshold probability:

$$G(E') = \begin{cases} 1 & (E' > E_d) \\ 0 & (E' < E_d) \end{cases} \quad (2)$$

and the total cross section for atom displacement (1) is described by the Darwin–Rutherford formula

$$\sigma_d = \pi z^2 e^4 (1 - \beta^2)(E_m/E_d - 1)/m^2 c^4 \beta^4, \quad (3)$$

where z is the atomic number, e and m are the charge and mass of an electron, c is the speed of light, $\beta = v/c$, v is the electron velocity and E_m is the maximum recoil energy. In a direct collision, the maximum energy E_m transferred to a silicon single crystal of atom mass M_{Si} is

$$\begin{aligned} E_m &= 2E(E + 2m_0c^2)/M_{Si}c^2 \\ &= 76.7E(E + 1.02) \end{aligned} \quad (4)$$

(E_m is in eV for E in MeV). If the maximum recoil energy E_m is close to the threshold energy for displacement energy E_d, then only the primary head-on-collision event produces point defects (separated Frenkel V–I pair formation). Therefore, the incident electron energy E can be calculated from (3) and (4) and must satisfy

$$E^2 + 1.02E - 0.013E_d = 0. \quad (5)$$

For silicon, E_d (which depends on the incident-beam direction) at near room temperature is in the range 11–22 eV (Vinetskii & Kholodar, 1986). From (5), the incident-electron energy to produce point defects must be more than 125–229 keV and less than the energy for static observation of separated Frenkel pairs. This range of incident energy is required to produce point defects by primary head-on collision with an incident electron. For static observation of separated Frenkel pairs, it is desirable to cool the silicon specimen by liquid helium. If the energy transferred to the atom by an incident electron is much higher than E_d, the number of displaced atoms must be calculated by considering the multiplication of knock-on atoms. Kinchin & Pease (1955) calculated the total number of displaced atoms by taking into account the multiplication of knock-on atoms due to secondary, tertiary *etc.* knock-ons caused by the primary knock-on atom, that is

$$N_d(E') = \begin{cases} 1 & (E_d \leq E' \leq 2E_d) \\ E'/2E_d & (2E_d < E'). \end{cases} \quad (6)$$

From (4), the maximum transferable energy for an 800 keV incident electron is 112 eV and, if we suppose that $E_d = 21$ eV (Corbett & Watkins, 1965), $N_d < 3$ atoms. As most collisions between a fast incident electron and the primary knock-on atom are not direct, that is

$$E'(\theta) = E_m \sin^2(\theta/2), \quad (7)$$

where θ is a scattering angle of the fast incident electron by the primary knock-on atom, $N_d < 3$. If the incident beam is set parallel to Si⟨110⟩, a small SFT could be produced by this multiplication knock-on process but, as the incident beam is converged to increase the current density, the SFT could be produced at a very early stage of the damage process.

The authors thank Professors P. B. Hirsch, H. Endoh, M. J. Whelan and A. Howie and Drs N. Ajika, M. Tomita, S. Horiuchi, W. O. Saxton and P. W. Hawkes for their advice and discussions. The authors acknowledge financial support from the Ministry of Education, Science and Culture and the Japan Society for the Promotion of Science for the award of a Postdoctoral Fellowship for research abroad (1993–1995) (MA).

References

Ajika, N., Hashimoto, H. & Takai, Y. (1985). *Phys. Status Solidi A*, **87**, 235–252.

Burgers, J. M. (1939). *Proc. Acad. Sci. Amsterdam*, **42**, 293–325.

Bursill, L. A. & Jun, S. G. (1984*a*), *Optik (Stuttgart)*, **66**, 251–276.

Bursill, L. A. & Jun, S. G. (1984*b*). *Ultramicroscopy*, **13**, 191–204.

Coene, W., Bender, H. & Amelinckx, S. (1985). *Philos. Mag.* A**52**, 369–381.

Corbett, J. W. & Watkins, G. D. (1961). *Phys. Rev. Lett.* **7**, 314–316.

Corbett, J. W. & Watkins, G. D. (1965). *Phys. Rev. A*, **138**, 555–560.

Fields, P. M. & Cowley, J. M. (1978). *Acta Cryst.* A**34**, 103–112.

Gibson, J. M. & McDonald, M. L. (1987). *Mater. Res. Soc. Symp. Proc.* **82**, 109–113.

Glaisher, R. W. & Spargo, A. E. C. (1983). *EMAG*, pp. 185–188.

Hashimoto, H., Makita, Y., Yokota, Y., Ikuta, T., Hashimoto, M. & Hetherington, C. J. D. (1991). *Ultramicroscopy*, **39**, 171–179.

Hashimoto, H., Takai, Y., Ajika, N., Yokota, Y. & Endoh, H. (1982). Proceedings of the Yamada Conference, pp. 698–701.

Hirsch, P. B., Howie, A., Nicholson, R. B., Pashley, D. W. & Whelan, M. J. (1965). *Electron Microscopy of Thin Crystals*. London: Butterworths.

Kinchin, G. H. & Pease, R. S. (1955). *Rep. Prog. Phys.* **18**, 1–51.

Krakow, W., Chang, A. L. J. & Sass, S. L. (1977). *Philos. Mag.* **35**, 575–592.

Rose, A. (1948). *Adv. Electron.* **1**, 131–166.
Saldin, D. K. & Whelan, M. J. (1979). *Philos. Trans. R. Soc. London Ser. A*, **292**, 513–537.
Saxton, W. O. (1978). *Computer Techniques for Image Processing in Electron Microscopy*. New York: Academic Press.
Takai, Y., Ajika, N. & Hashimoto, H. (1982). Proceedings of the Yamada Conference, pp. 702–704.
Takai, Y., Zakharov, N. D. & Hashimoto, H. (1982). Proc. ICEM-10, pp. 375–376.
Vinetskii, V. L. & Kholodar, G. A. (1986). *Physics of Radiation Effects in Crystals*. Amsterdam: North-Holland.
Yoffe, E. H. (1960). *Philos. Mag.* **5**, 161–175.
Zakharov, N. D., Pasemann, M. & Rozhanski, V. N. (1982). *Phys. Status Solidi A*, **71**, 275–281.